Computers and Chemical Engineering 199 (2025) 109113

Contents lists available at ScienceDirect

Computers and Chemical Engineering

journal homepage: www.elsevier.com/locate/cace

The SABYDOMA Safety by Process Control framework for the production of functional, safe and sustainable nanomaterials

Argyri Kardamaki [a], Athanassios Nikolakopoulos [a], Mihalis Kavousanakis [a], Philip Doganis [a], Matt Jellicoe [b], William Stokes [b], Vesa Hongisto [e], Matthew Simmons [b], Thomas W. Chamberlain [b], Nikil Kapur [c], Roland Grafström [d,e], Andrew Nelson [b], Haralambos Sarimveis [a,*]

[a] School of Chemical Engineering, National Technical University of Athens, 9 Iroon Polytechniou Street, Athens, 15772, Greece
[b] Institute of Process Research and Development, School of Chemistry and School of Chemical and Process Engineering, University of Leeds, Leeds, LS2 9JT, United Kingdom
[c] School of Mechanical Engineering, University of Leeds, Leeds, LS2 9JT, United Kingdom
[d] Institute of Environmental Medicine, Karolinska Institutet, Nobels väg 13, Stockholm, 17177, Sweden
[e] Misvik Biology Ltd, Karjakatu 35 B, Turku, FI-20520, Finland

ARTICLE INFO

Keywords:
Safety-by-process-control
Model Predictive Control
Nanomaterial synthesis
Safe and sustainable by design

ABSTRACT

The production of nanomaterials (NMs) has gained significant attention due to their unique properties and versatile applications in fields such as medicine, energy, and electronics. However, ensuring the large-scale synthesis of safe and sustainable NMs while maintaining their functionality remains a critical challenge. This study introduces the Safety by Process Control (SbPC) framework, a novel methodology integrating dynamic first-principles modeling, Model Predictive Control (MPC), and real-time safety monitoring. The framework employs a physics-based population balance model with a Method Of Moments (MOM) approximation to predict the evolution of key NM properties. A toxicity inferential sensor, built on experimental data, is integrated to facilitate real-time hazard assessment. The efficiency of the proposed framework is demonstrated using a continuous silver nanoparticle (Ag NP) production system as a case study. The proposed approach ensures the production of high-quality, safe, and sustainable NMs, aligning with Safe and Sustainable by Design (SSbD) principles and addressing gaps in current NM manufacturing processes. The framework's adaptability to other NM types highlights its potential as a transformative tool for sustainable nanotechnology.

1. Introduction

Nanomaterials (NMs) constitute a class of advanced materials that exhibit remarkable properties and have found promising applications in various fields, including medicine, energy conversion, catalysis, sensing, nanocomposite engineering and cosmetics (Sasidharan et al., 2019; Saldanha et al., 2017). While significant advancements have been made in their fabrication and fundamental studies, their widespread adoption has been hampered by challenges in scalable, reproducible synthesis and increasing concerns on the safety of NMs for human health and the environment (Sánchez Jiménez et al., 2022; Mech et al., 2022). In alignment with the Safe and Sustainable by Design (SSbD) principles, it is essential to acheive efficient, large-scale production of high-quality functional NMs while simultaneously addressing potential safety and sustainability concerns (OECD, 2022; Caldeira et al., 2022).

Among the various types of NMs, silver nanoparticles (Ag NPs) hold a distinct position, demonstrating potential applications in a variety of fields, including medicine, agriculture, catalysis, optics, and electronics (Abou El-Nour et al., 2010; Prabhu and Poulose, 2012; Beyene et al., 2017). Various approaches have been developed for the synthesis of Ag NPs, each with distinct advantages and limitations (Iravani et al., 2014). Physical and photochemical techniques often demand specialized equipment and must be controlled continuously (Jara et al., 2021), while biological methods may have limited reproducibility (Sharma et al., 2022). Chemical methods, in contrast, offer a versatile and scalable platform for producing high-purity Ag NPs under mild conditions. Specifically, chemical reduction in organic solvents or water can yield Ag NPs with controlled morphology and size distribution (Yaqoob et al., 2020). Chemical methods for synthesizing Ag NPs are widely employed

* Corresponding author.
E-mail address: hsarimv@central.ntua.gr (H. Sarimveis).

https://doi.org/10.1016/j.compchemeng.2025.109113
Received 2 December 2024; Received in revised form 8 February 2025; Accepted 24 March 2025
Available online 6 April 2025

due to their high efficiency, convenience, and low cost. Typical chemical approaches involve three types of reagents: metal-based precursors, capping oxidants, and reducing agents.

The demand for Ag NPs is growing rapidly (Syafiuddin et al., 2017) but cannot be met by current batch production methods (Cristaldi, 2020). This necessitates a transition to continuous production (Długosz and Banach, 2019; Gacem and Abd-Elsalam, 2022; Makgwane and Ray, 2014). Controllable and tunable Ag NPs synthesis using microreactors has attracted increasing research interest (Prakash et al., 2020; Zhu et al., 2021). High-throughput microreactors enable synthesis with precise control of the NPs morphological characteristics, while optimizing reactor geometry addresses laminar flow challenges and enables NP synthesis with narrow size distributions (Gao et al., 2020). Recently, microfluidic-based synthesis systems have been introduced to enable the controlled production of spherical Ag NPs with tunable sizes for various applications (Pinho and Torrente-Murciano, 2020). Furthermore, a self-regulating multistage Ag NP synthesis system has been developed for the production of tunable particle sizes (4–100 nm), incorporating real-time feedback control to overcome reproducibility issues and maintain stable NM production for long reaction times (Pinho and Torrente-Murciano, 2021).

The production of Ag NPs has many common characteristics with the process of crystallization. It is a multifaceted process governed by several fundamental mechanisms, including nucleation and growth. Population balance modeling (PBM) offers a comprehensive and dynamic understanding of NP size distribution evolution over time (Ramkrishna, 2000; Randolph, 2012; Ramkrishna and Singh, 2014). In this approach, a population of NPs is viewed as a continuum, accounting for various mechanisms such as nucleation and growth. The rates of these processes are formulated with appropriate mathematical equations, enabling accurate predictions of crystal size distribution under varying conditions (Vetter et al., 2013). Solving Population Balance Equations (PBEs) poses challenges, primarily due to the discretization of the internal coordinate space (e.g., NP diameter), which leads to prohibitive for control applications computational times. Numerical methods, such as the Finite Volume Method (FVM) (Filbet and Laurençot, 2004; Kumar et al., 2009) and the Cell Average Technique (CAT) (Kumar et al., 2008), are commonly employed for their solution. Selecting an efficient numerical method depends on specific problem characteristics, including particle interactions, size distribution complexity, and available computational resources. Monte Carlo simulations offer a particle-level perspective, particularly useful for simulating multivariate population balances (Lin et al., 2002). The Method of Moments (MOM) involves transforming PBEs into equations in terms of the moments of the number density function (Randolph, 2012). Hulburt and Katz (Hulburt and Katz, 1964) argue for tracking lower-order moments instead of the complete number density function, simplifying the complex population balance equation into a system of simple differential equations dependent only on time and space. Moments-based methods offer the advantage that low-order moments are related to physically meaningful and generally measurable macroscopic properties. Quadrature-based Methods of Moments (QMOM) (McGraw and Wright, 2003) approximate the density function using a quadrature formula, aiming to close the infinite system of moment equations by selecting a finite set of quadrature weights and abscissas. The first implementations of QMOM for calculating Ag NPs distributions in a microtubular reactor combined multiphase model theory, and kinetic theory of granular flow (Liu et al., 2014; Bal and Bandyopadhyaya, 2018). The method has been also used to assess mixing regimes and reactor configurations by predicting the size of Ag NPs synthesized in flow reactors (Casado et al., 2023; Pico et al., 2023). The Direct Quadrature Method of Moments (DQMOM) (Marchisio and Fox, 2005) directly solves for the quadrature weights and abscissas involved in the moment approximation. In this study, the focus is on developing a first-principles mathematical model to efficiently compute physically meaningful quantities, such as the mean and the variance of the Ag NPs size by employing the MOM approximation for the numerical computations. Nucleation and growth are considered as the main mechanisms, omitting secondary phenomena like aggregation and breakage. This allows for deriving closed forms for the lower-order moments of the NP distribution, facilitating their direct coupling with the fluid flow in the series of Plug Flow Reactors (PFRs) used for Ag NP production.

The toxicity of Ag NPs is size dependent: smaller NP sizes generally lead to higher toxicity (Kong et al., 2020; Waktole, 2023; Cho et al., 2018; Noga et al., 2023; Akter et al., 2018). The increased toxicity of smaller Ag NPs can be attributed to their significantly larger surface-to-volume ratio and particle concentration, which increases their potential interaction with biomolecules and triggers adverse biological responses. The toxicity of Ag NPs is also influenced by their shape, as demonstrated by the presence of active metallic facets (Tak et al., 2015), or aspect ratio (Acharya et al., 2018). It has been shown that spherical Ag NPs exhibit higher toxicity compared to other geometric configurations, due to their higher circularity (Panzarini et al., 2018; Auclair and Gagné, 2022). A combined approach of engineering NP toxicity to desired levels by modifying their size and surface is presented by Zhang et al. (2022). In this work, we employ the ToxScore metric (Hongisto et al., 2019), for assessing the toxicity of Ag NPs. ToxScore provides a single aggregated toxicity score by combining multiple toxicity endpoints derived from five assays conducted on cell line models.

So far, the challenge of controlling the morphological characteristics of Ag NPs while simultaneously ensuring the safety of the end product for human health and the environment during continuous Ag NP production has not been fully addressed. This work demonstrates that by utilizing an inferential toxicity sensor, which predicts the ToxScore metric as a function of the NP mean diameter, it is possible to perform real-time predictions of health hazards. The mean diameter of the produced NPs can be estimated in real-time from online experimental measurements of UltraViolet–Visible (UV–Vis) absorption spectra. More specifically, the wavelength on the UV spectrum corresponding to the peak absorbance can be converted to the average NP diameter using an approximation of the Mie Theory (Mie, 1908; Eremin, 2005). Mie theory provides a solution to Maxwell's equations for the interaction of light with a spherical particle, taking into account the particle's size, refractive index, and the wavelength of the incident light. Mie theory is particularly applicable to the scattering and absorption of light by particles comparable in size to the wavelength of the light, such as in the case of NPs (Gupta et al., 2018; Niskanen et al., 2019). It provides size estimations which are in agreement with size measurement obtained from Transmission Electron Microscopy (TEM), particularly for metal NPs, like silver (Baset et al., 2011).

The control algorithm used in this work to regulate the production process of Ag NPs is Model Predictive Control (MPC). MPC is an advanced control strategy extensively used across various industries due to its capability to manage complex processes with multiple variables and constraints (Camacho et al., 2007). This capability makes MPC particularly effective for systems that require balancing competing objectives to achieve optimal performance.

To the best of the authors' knowledge, the use of MPC in the production of Ag NPs has not been addressed in the literature. However, several studies have proposed the application of MPC in crystallization processes, which present challenges similar to those encountered in NM synthesis. For example, Kwon et al. (2014) developed a comprehensive framework for modeling and controlling crystal shape during continuous protein crystallization. Their approach utilized MPC to produce crystals with a desired shape distribution. They employed a MOM model to approximate the dominant behavior of a PBE, which described the crystal volume distribution in a mixed suspension mixed product removal crystallizer. This moment model was then used to design an MPC controller capable of manipulating jacket temperature to address changes in set-point values and disturbances effectively. Similarly, Tahir et al. (2017) explored the application and challenges

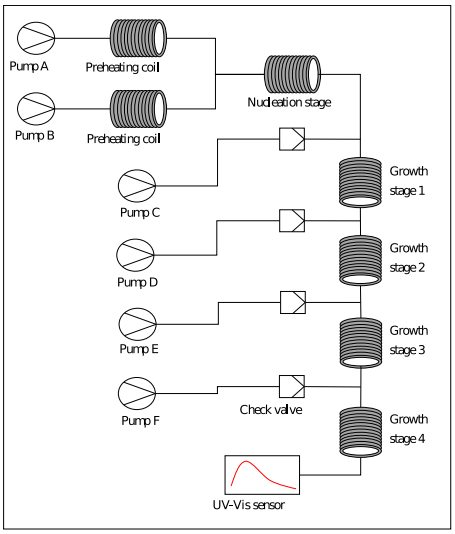

Fig. 1. Configuration of the Ag NPs production system.

of MPC in continuous oscillatory baffled crystallization reactors, which are an intensified form of PFRs.

The proposed SbPC methodology is illustrated through a case study conducted as part of the SABYDOMA Horizon 2020 research project (Nelson, 2022). The study focuses on the control of the SABYDOMA Lead Demonstrator, which is a continuous lab-scale Ag NPs microfluidics production process. This process involves a series of PFRs integrated with an advanced online sensor for nanotoxicity screening (Owen et al., 2020). The precursor used is silver nitrate ($AgNO_3$), while sodium citrate (SC) and tannic acid (TA) solutions act as reducing and capping agents under low-temperature conditions. This combination offers an efficient and environmentally friendly method for controlling the size and morphology of Ag NPs (Cheng et al., 2016).

It is demonstrated that the application of the proposed methodology effectively addresses the challenge of regulating the morphological and safety characteristics of Ag NPs produced in the continuous SABYDOMA process. Additionally, it is illustrated that the proposed SbPC framework provides a systematic approach for implementing the SSbD principles at the production stage, in alignment with Pillar 2 of the OECD SSbD description (OECD, 2022).

2. Model of the process

2.1. Process description - The Ag NPs production system

The configuration of the Ag NPs production system is described in Fig. 1. The Ag NPs are produced by a system of five PFRs in series immersed in a heated water bath. The first PFR is fed with an $AgNO_3$ and a SC-TA solution and is dedicated to the nucleation process. The subsequent four PFRs serve as growth stages, with each one being fed with an $AgNO_3$ solution of the same concentration.

2.2. System kinetics and first principles population balance model

In this section, a first principles approach is employed to model the formation of Ag NPs using the Finke–Watzky (F–W) two-step mechanism (Thanh et al., 2014). This mechanism assumes a slow continuous nucleation (Eq. (1)) followed by a fast autocatalytic surface growth (Eq. (2)) (Sandoe et al., 2019):

$$A \xrightarrow{k_n} B, \tag{1}$$

$$A + B \xrightarrow{k_g} B, \tag{2}$$

where A represents nuclei, and B represents NPs.

The resulting kinetic curves exhibit a sigmoidal shape due to the F–W two-step model, with nucleation rate constant, k_n, and surface growth rate constant, k_g (Bentea et al., 2017). Experimental observations on Ag NPs production show that increasing SC concentration leads to smaller particle sizes.

In addition, higher concentrations of metal atoms result in larger Ag NP sizes, favoring growth over nucleation. The presence of the capping agent, TA, also influences growth kinetics, with higher concentrations leading to the formation of smaller NPs. Considering these factors, the NP growth rate is formulated as follows:

$$G \equiv G(D) = G_o(1 + \alpha D), \tag{3}$$

where $G_o = k_g C_A C_{SC}^{-1} C_{TA}^{-1}$, and α is a temperature dependent parameter quantifying size-dependent growth rate; C_A, C_{SC}, C_{TA} denote concentration of metal atoms, SC and TA, respectively. Here, for simplification purposes a linear relation between growth rate and diameter size is assumed. The growth rate constant, k_g, follows an Arrhenius equation formulating its temperature dependence:

$$k_g = k_{g,o} \exp\left(-E_{a,g}/RT\right), \tag{4}$$

where $k_{g,o}$ is the pre-exponential factor, $E_{a,g}$ is the activation energy of growth kinetics, R is the gas constant and T denotes the temperature.

For nucleation, a simple linear relation with the concentration of diluted precursor, C_{AgNO_3}, is assumed:

$$J = k_n C_{AgNO_3}. \tag{5}$$

The nucleation rate constant, k_n exhibits an Arrhenius-type dependence on temperature:

$$k_n = k_{n,o} \exp\left(-E_{a,n}/RT\right), \tag{6}$$

where $k_{n,o}$ is the pre-exponential factor and $E_{a,n}$ denotes the activation energy of nucleation kinetics.

In this study, the population dynamics of NPs are modeled, each characterized by its diameter, D. Denoting the number density function of Ag NPs with $n(\vec{x}, D, t)$, the population balance model (Eq. (7)) describes the evolution of n in flow, neglecting breakage and aggregation processes:

$$\frac{\partial n}{\partial t} + \nabla \cdot \left(\vec{v} n\right) + \frac{\partial}{\partial D}(Gn) = 0 \rightarrow \frac{\partial n}{\partial t} + v_x \frac{\partial n}{\partial x} + \frac{\partial}{\partial D}(Gn) = 0, \tag{7}$$

where $\vec{v} = v_x$ corresponds to the fluid velocity in the plugflow reactor, assuming a one-dimensional flow (the fluid velocity within each pluglow reactor is uniform). The PBE is complemented by appropriate initial and boundary conditions.

In our system, it is considered that initially no particles exist in the plug flow reactors volume, $n(x, D, 0) = 0$, and particles with $D = 0$ are produced through nucleation, i.e,:

$$n(x, 0, t) = J/G(0), \tag{8}$$

where J denotes the nucleation rate (given by Eq. (5)), and $G(0)$ is the growth rate at size $D = 0$: $G(0) = G_o$. The particle PBE is coupled with mass balance equations for the diluted species of the system, and in particular for the capping agent, TA, and the SC species:

$$\begin{aligned} \frac{\partial C_{TA}}{\partial t} + v_x \frac{\partial C_{TA}}{\partial x} &= 0, \\ \frac{\partial C_{SC}}{\partial t} + v_x \frac{\partial C_{SC}}{\partial x} &= 0. \end{aligned} \tag{9}$$

Finally, the mass balance for the solute is written as (Bosetti and Mazzotti, 2019):

$$\frac{\partial C_{AgNO_3}}{\partial t} + v_x \frac{\partial C_{AgNO_3}}{\partial x} + \frac{\rho_c k_v}{MW} \frac{\partial \mu_3}{\partial t}, \tag{10}$$

where ρ_c is the density of NPs, k_v is the shape factor of the NPs, MW denotes the molecular weight, and $\mu_3 \equiv \int_0^\infty D^3 n(x, D, t) \mathrm{d}D$, corresponds to the third order moment of the NP population.

2.3. Method of Moments (MOM) model

Solving the system of Eqs. (7)–(10) is computationally intensive, prompting the utilization of average or total quantities to represent particle distributions. Lower order moments of the distribution function, n, offer a practical alternative, describing useful statistics of the NP population. These statistics include the average diameter, the standard deviation from the average diameter, and the mass concentration of NPs.

For the system under study, the PBE has one spatial dimension ($\vec{x} = x$) and one size dimension (the diameter, D), whereas the mass balances are one-dimensional (assuming negligible energy and momentum gradients). One can alleviate the extra dimension for the solution of the population balance model (diameter, D), by deriving the corresponding equations that describe the dynamics of the populations statistics, i.e. of the lower order moments of the NP distribution. Multiplying Eq. (7) by D^j and integrating from 0 to ∞ with respect to D, yields equations describing the dynamics of moments, μ_j:

$$\frac{\partial \mu_j}{\partial t} + v_x \frac{\partial \mu_j}{\partial x} + (Gn)\Big|_0^\infty = 0 \xrightarrow[n(x,D\to\infty,t)=0]{Eqs.\ (3),(8)} \tag{11}$$

$$\frac{\partial \mu_0}{\partial t} + v_x \frac{\partial \mu_0}{\partial x} - J = 0, \tag{12}$$

$$\frac{\partial \mu_j}{\partial t} + v_x \frac{\partial \mu_j}{\partial x} - jG_o\left[\mu_{j-1} + \alpha\mu_j\right] = 0, \quad j \geq 1 \tag{13}$$

where J denotes the nucleation rate formulated using Eq. (5); G_o, α denote the zero diameter growth rate, and the proportionality constant that quantifies the linear dependence of growth rate, G, on diameter, D (see Eq. (3)).

Furthermore, the parameter α is assumed to follow an Arrhenius-type dependence on temperature:

$$\alpha(T) = \alpha_o e^{-\frac{E_{\alpha,a}}{RT}}. \tag{14}$$

Eqs. (12)–(13) form a closed set describing the evolution of moments, μ_j, dependent on spatial dimension, x and time, t.

Given the above, one can track any number of moments; by increasing the number of tracked moments, the reconstruction of number density function, n is more accurate, however the computational cost also increases. In practice, only the lower order moments, μ_0, μ_1, μ_2, μ_3, are of particular interest, representing the number, average size, mean area and mass of NPs, respectively.

In this work, the evolution of several parameters is simulated, including:

- Moments up to 3rd order (μ_3): Eqs. (12)–(13) for $j = 0, 1, 2, 3$
- The mass balance equations for TA and SC: Eqs. (9)
- The mass balance of the solute ($AgNO_3$): Eq. (10)

Assuming the inflow stream to the first reactor ($x = 0$) does not contain any seeds, Dirichlet boundary conditions are imposed for each moment of the NP distribution, i.e.:

$$\mu_j(0,t) = 0, \quad j = 0, 1, 2, 3 \tag{15}$$

For the solute concentration, C_{AgNO_3}, a Dirichlet type boundary condition is also imposed:

$$C_{AgNO_3}(0) = C^0_{AgNO_3}, \tag{16}$$

where $C^0_{AgNO_3}$ is the concentration of $AgNO_3$ at the inlet of the 1st PFR. The value of the state variable C_{AgNO_3}, at the inlets of reactors #2, #3, #4 and #5 are determined by the mass balances at the junctions where fresh $AgNO_3$ solution is introduced to each reactor. At the mixing point the distribution of the particles n is not affected by the addition of $AgNO_3$ solution (it only affects the concentration of the population of NPs in the stream).

The main interest of this work lies in monitoring the average diameter of produced NPs:

$$\bar{D} = \frac{\mu_1}{\mu_0}, \tag{17}$$

and the standard deviation of the NP population:

$$\sigma = \left(\frac{\mu_2}{\mu_0} - \bar{D}^2\right)^{\frac{1}{2}}. \tag{18}$$

3. Model predictive control framework

MPC is a control strategy that solves an online optimization problem at each sampling instant to compute the optimal control action. This control methodology requires a dynamic model of the plant to predict the system's future behavior over a finite time horizon, hence the name 'Model Predictive Control'. MPC stands out among other control strategies because it can easily handle multi-input multi-output systems and incorporate multiple constraints on the input and output variables. The constraints imposed by the algorithm ensure that all input signals remain within the capacities of the system actuators, and the output variables do not violate the bounds specified by production protocols. The objective function includes the errors between model predictions and the desired set-points, as well as the incremental changes of the manipulated inputs. The optimization problem is reformulated and solved at each time step, incorporating feedback from the plant, with the controller implementing only the first control action from the sequence of computed actions. The rolling-horizon concept of MPC is presented graphically in Fig. 2.

3.1. Dynamic matrix control

This study employs Dynamic Matrix Control (DMC) as the control algorithm, which is a popular MPC variant. In DMC, discrete time step-response models of the plant are integrated in the control algorithm to provide the predictions for the system's future behavior (Tatjewski, 2007; Camacho et al., 2007; Mulholland, 2016). The step response model that describes the model output, $y(t)$, is given by:

$$y(t) = \sum_{i=1}^{\infty} g_i \Delta u(t-i), \tag{19}$$

where g_i are the step response coefficients and Δu is the change of the manipulated variable u between two consecutive discrete time instances.

In systems that reach a steady state over a finite horizon, l_{pin}, the prediction of the output at time instant k, $\hat{y}(t+k|t)$, takes the following form:

$$\hat{y}(t+k|t) = \sum_{i=1}^{k} g_i \Delta u(t+k-i) + \sum_{i=1}^{l_{pin}} (g_{k+i} - g_i)\Delta u(t-i) + y_m(t) - y_{ss}, \tag{20}$$

where $y_m(t)$ is the current output measurement and y_{ss} is the steady state at which the step response model has been derived. Measured disturbances can be incorporated into Eq. (20) as additional input variables that cannot be manipulated. In this case, the prediction of the output at each time instant $t+k$ can be described by:

$$\hat{y}(t+k|t) = \sum_{i=1}^{k} g_i \Delta u(t+k-i) + \sum_{i=1}^{k} g'_i \Delta d(t+k-i) + \sum_{i=1}^{l_{pin}} (g_{k+i} - g_i)\Delta u(t-i) + \sum_{i=1}^{l_{pin}} (g'_{k+i} - g'_i)\Delta d(t-i) + y_m(t) - y_{ss}, \tag{21}$$

where g'_i is the step response coefficient for the measured disturbance prediction model at each sampling instance and Δd is the change of

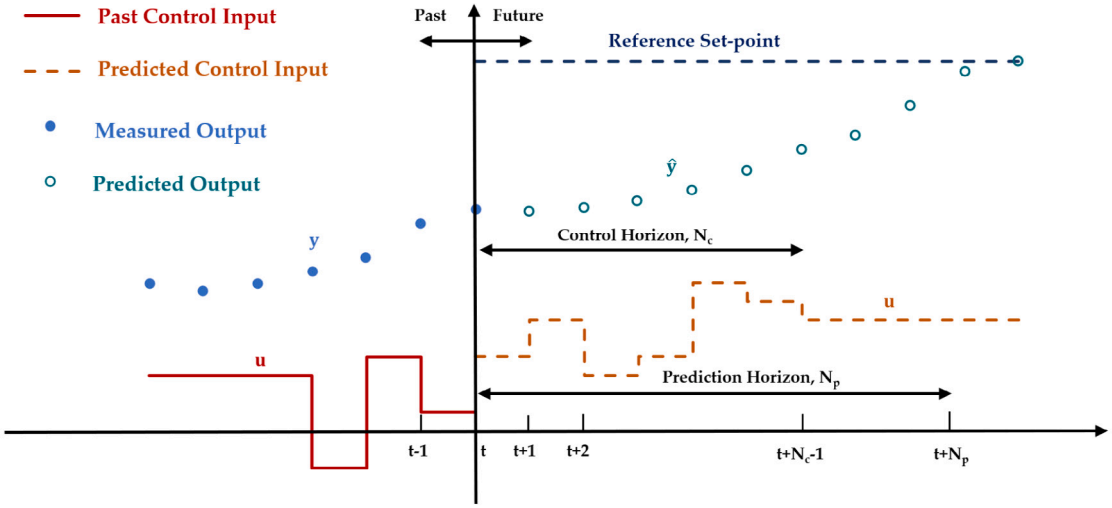

Fig. 2. The rolling horizon concept of MPC.

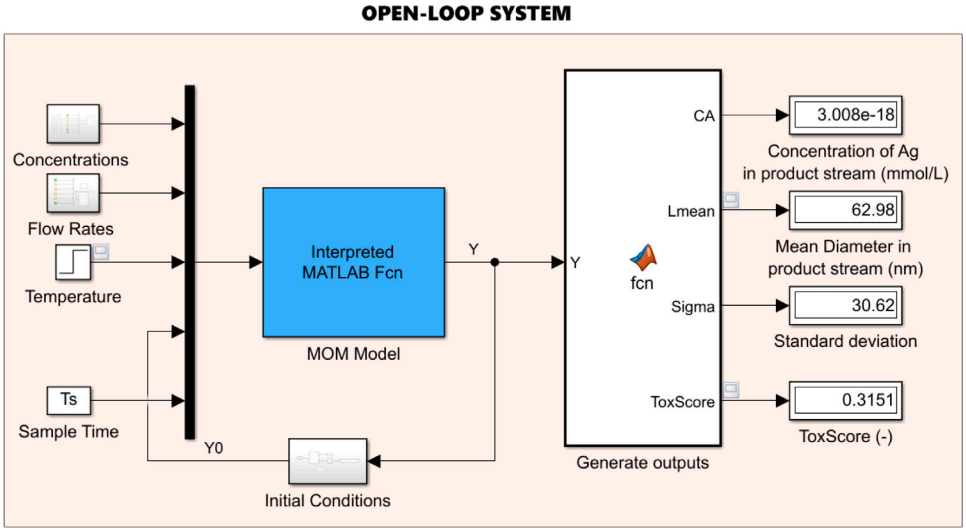

Fig. 3. Open-Loop dynamic simulator.

the measured disturbance d between two consecutive discrete time instances.

The DMC algorithm determines the optimal sequence of future manipulated variables over the control horizon $(\Delta u(t), \dots, \Delta u(t + N_c))$ by minimizing the quadratic objective function:

$$\min_{(\Delta u(t),\dots,\Delta u(t+N_c))} \left\{ \sum_{k=1}^{N_p} \left\| \hat{y}(t+k|t) - y_{sp} \right\|_Q^2 + \sum_{k=0}^{N_c} \left\| \Delta u(t+k) \right\|_R^2 \right\}, \tag{22}$$

where $\hat{y}(t + k|t)$ is the output prediction at time instance $t + k$ given by Eq. (20) or Eq. (21), y_{sp} is the desired set-point value, N_p and N_c correspond to the prediction and control horizon respectively and Q, R are positive definite matrices weighting the output deviations from the set-point and the increments of the manipulated variables, respectively. The increments of the manipulated variables, Δu, at each time instance $t + k$ are defined as:

$$\Delta u(t+k) = u(t+k) - u(t+k-1), k = 0, \dots, N_c \tag{23}$$

The manipulated and the controlled variables are constrained within upper and lower bounds with the following inequalities:

$$u_{min} \le u(t+k) \le u_{max}, k = 0, \dots, N_c, \tag{24}$$

$$y_{min} \le \hat{y}(t+k|t) \le y_{max}, k = 1, \dots, N_p \tag{25}$$

Hard constraints, as described in Eqs. (24)–(25), impose conditions on the variables that must be satisfied at all times. However, these conditions may lead to infeasibility issues if no solution exists that satisfies all constraints. To address this problem, hard constraints can be replaced by soft constraints, which set conditions that are desirable to satisfy as much as possible, but also allow for violations as a compromise to ensure a feasible solution to the optimization problem.

Soft constraints on the predicted output variables can be incorporated into the control algorithm using slack variables. This modification alters the objective function of the DMC algorithm as follows:

$$\min_{(\Delta u(t),\dots,\Delta u(t+N_c))} \left\{ \sum_{k=1}^{N_p} \left\| \hat{y}(t+k|t) - y_{sp} \right\|_Q^2 + \sum_{k=0}^{N_c} \left\| \Delta u(t+k) \right\|_R^2 + \right.$$
$$\left. + W_{min} \sum_{k=1}^{N_p} \epsilon_{min}(t+k) + W_{max} \sum_{k=1}^{N_p} \epsilon_{max}(t+k) \right\}, \tag{26}$$

Table 1
Estimated kinetic parameter values.

Kinetic Constant	$k_{n,o} = 1.2 \cdot 10^{-4}$ nm/(min mM)
Diameter Dependence Factor	$a_o = 1.0 \cdot 10^{-3}$ 1/nm
Kinetic Constant	$k_{g,o} = 24$ (nm mM)/min
Activation Energy	$E_{a,n} = 3.2 \cdot 10^5$ kJ/mol
Activation Energy	$E_{a,a} = 4.8 \cdot 10^5$ kJ/mol
Activation Energy	$E_{a,g} = 5.5 \cdot 10^5$ kJ/mol

where W_{min}, W_{max} are weights to penalize soft constraint violations and $\epsilon_{min}, \epsilon_{max}$ are the non-negative slack variables:

$$\epsilon_{min}(t+k), \epsilon_{max}(t+k) \geq 0, k = 1, \dots, N_p. \tag{27}$$

In this case, Eq. (25) is adjusted accordingly to include $\epsilon_{min}, \epsilon_{max}$:

$$y_{min} - \epsilon_{min}(t+k) \leq \hat{y}(t+k|t) \leq y_{max} + \epsilon_{max}(t+k), k = 1, \dots, N_p. \tag{28}$$

This structure of the optimization problem enables the controller to assign values other than zero to ϵ_{min} and ϵ_{max}, allowing for violation of the hard constraints in Eq. (25) to ensure that a feasible solution is acquired at every time step during optimization.

4. Case study

In this case study, our goal was to implement the modeling and control methodologies described in the previous sections to design a complete MPC framework, where the developed MOM model serves as a representation of the Ag NPs actual production plant.

4.1. Kinetic parameters estimation

The kinetic parameter values of G_o and J in the population balance model, including the factor introduced for the diameter dependence $a(T)$, were estimated by applying the Thompson Sampling Efficient Multiobjective Optimization (TSEMO) algorithm (Bradford et al., 2018) on steady state experimental data collected from the SABYDOMA Lead Demonstrator process. For each experiment $k = 1, \dots, K$, the available input data included the flow rates and concentrations of the $AgNO_3$, SC and TA solutions (in uL/min and mmol/L respectively), as well as the temperature (in °C). The output data consisted of the UV spectrum and the concentration of Ag NPs at the reactor outlet. The average experimental NP diameter $D_{\text{exp},k}$ (in nm) was estimated by applying Mie Theory (Mie, 1908) on the UV spectrum, as described in the introduction section.

Two objectives were considered:

1. Minimizing the sum of squared differences between the calculated (D_k) and experimental ($D_{\text{exp},k}$) Ag NP diameters:

$$f_1 = \sum_{k=1}^{K} (D_k - D_{\text{exp},k})^2$$

2. Minimizing the sum of squares of the concentration of $AgNO_3$ at the reactor outlet, which optimizes the yield:

$$f_2 = \sum_{k=1}^{K} \left(C_{\text{AgNO}_3,k} \right)^2$$

A large number of parameter samples were generated, with the sample size determined through computational experiments. The sample size was incrementally increased until no significant improvement in optimization results was observed. In the resulting Pareto front, f_2 reached its minimum value of 0 for several vectors of the kinetic parameters $\left[k_{n,o} \quad a_o \quad k_{g,o} \quad E_{a,n} \quad E_{a,a} \quad E_{a,g}\right]$. Among these, the parameter vector selected was the one that minimized the first objective, f_1. The selected solution from the Pareto front is presented in Table 1.

4.2. Toxicity prediction model

Samples of the Ag NPs produced by the SABYDOMA Lead Demonstrator were characterized using TEM and evaluated regarding their toxicity using the ToxScore metric, which is a combination of five endpoints, namely: CellTiter-Glo (CTG) a cell viability assay, 8OHG, an assay for DNA oxidative damage, Caspase 3/7 to identify apoptotic cells, H2AX histone phosphorylation, which constitutes an early event in the cellular response against double-strand breaks (DSBs) of DNA and the DAPI assay for the detection of blue fluorescence upon binding to AT regions of DNA using a nuclear and chromosome counterstain (4,6-diamidino-2-phenylindole, DAPI). The NPs were screened using BEAS-2B cells in the aforementioned assays in the presence and absence of 10% serum with 0-, 6-, 24- and 72-hour exposure time points, in four biological replicates and eight concentrations for each compound. The ToxPi v2.3 software (Reif et al., 2010; Marvel et al., 2018) was used to process the experimental data and calculate the final integrated ToxScore metric. Experimental data were available for 8 Ag NPs of varying sizes. The limited number of experimental data points makes the dataset unsuitable for the application of advanced machine learning methods to train a model that relates the ToxScore metric to the NP diameter D, thus restricting the search to linear or low-order polynomial models. Models up to the 3rd order were trained on the dataset, leading to the final selection of a second-order polynomial model that achieves a high R^2 value (R^2=0.8801) with an Leave-one-out (LOO) cross-validation R^2_{LOO} value of 0.7413:

$$ToxScore = -3 \cdot 10^{-5} \cdot D^2 - 8 \cdot 10^{-4} \cdot D + 0.4845. \tag{29}$$

The model in Eq. (29) will be used within the control framework as an inferential sensor to predict toxicity based on the NP diameter.

4.3. Open-loop simulation platform

The MOM model and the ToxScore model were integrated in the MATLAB-Simulink environment to construct an open-loop dynamic simulator of the production process (Fig. 3). This simulator requires a set of process inputs (the temperature and the flow rates and concentrations of the $AgNO_3$, SC and TA solutions) and a sampling time to compute the mean diameter of the produced Ag NPs, its standard deviation and the concentration of remaining Ag in the product stream. The mean diameter of the produced Ag NPs serves as an input to the inferential sensor, which estimates the ToxScore value using Eq. (29). This setup results in a total of four plant outputs.

The model was integrated into an interactive simulation platform, which allows users to simulate changes to the inputs via the control panel interface (Fig. 4). The control panel includes knobs for defining the inputs and edit blocks for specifying the exact timing of each step change. The interface features multiple display blocks that show current values of the input and output variables, along with the initial steady-state values.

An illustrative simulation is presented next, where the system starts with a mean NP diameter of 62.98 nm and a ToxScore of 0.315 and undergoes a series of step changes at different time points:

1. +50% in $AgNO_3$ flow rate in PFR#3 at t = 5
2. +20% in SC concentration in PFR#1 at t = 15
3. -30% in TA concentration in PFR#1 at t = 35
4. -25% in SC/TA flow rate in PFR#1 at t = 65

The step changes are depicted graphically in Fig. 5. Fig. 6 presents the corresponding dynamic responses of the mean diameter and the ToxScore of the produced Ag NPs at the effluent stream. The dashed vertical lines 1–4 indicate the time at which each step change occurs.

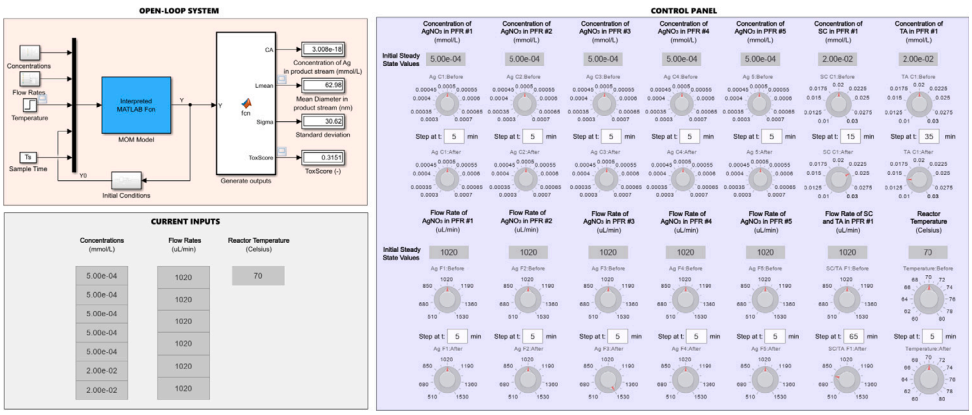

Fig. 4. Open-Loop simulation platform.

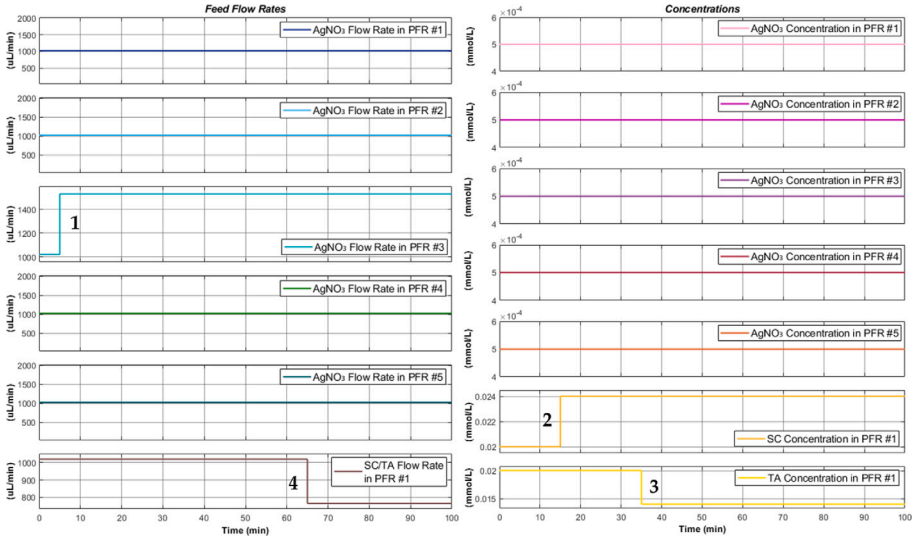

Fig. 5. Step changes in the flow rates and concentrations of the inlet streams.

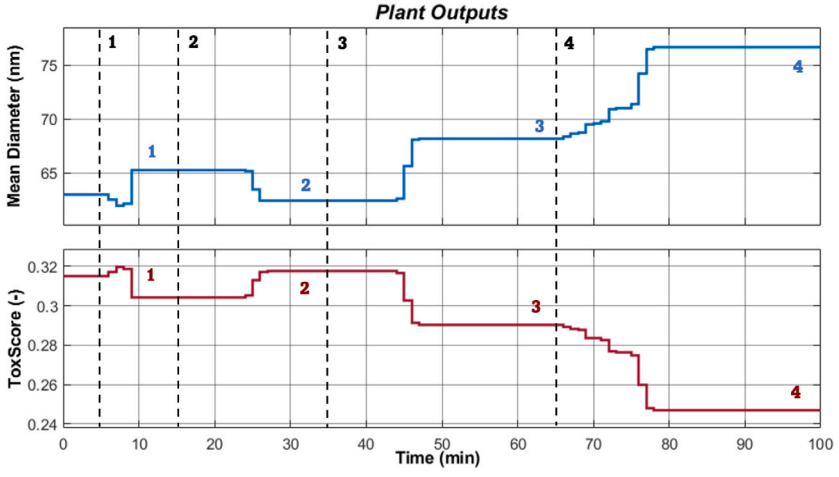

Fig. 6. Dynamic response of the mean diameter of Ag NPs and ToxScore corresponding to step changes in the flow rates and concentrations of the inlet streams.

4.4. Design of the control framework

The primary goal of this study was to develop a control framework for the production of Ag NPs that meets both functionality and safety specifications. To achieve this, the mean diameter of the Ag NPs in the product stream of the final PFR and the toxicity value of the produced Ag NPs (ToxScore) were designated as the controlled variables. While a set-point value for the mean diameter must be defined according to functionality specifications, the ToxScore — which serves as a metric for quantifying the toxicity of the Ag NPs — does not have a specific set-point. Instead, it is constrained by an upper bound, as higher ToxScore values indicate more toxic NPs based on Eq. (29). The manipulated

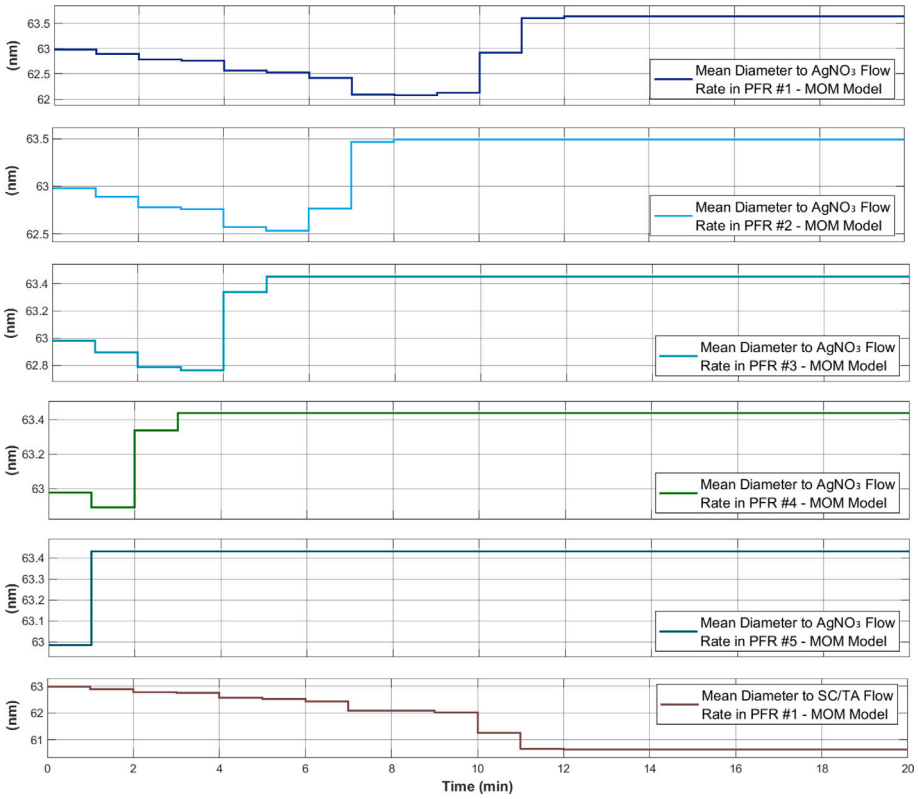

Fig. 7. Dynamic responses of NP mean diameter corresponding to 10% step changes in the manipulated variables.

variables in the control framework are the flow rates of all inlet streams into the five PFRs. The concentrations of these streams act as unmeasured disturbances.

Step response models, which are an integral part of DMC, were developed by introducing step changes to all manipulated variables in the open-loop simulator and simulating the dynamic effects on the mean diameter of the produced Ag NPs. More specifically, +10% step changes were introduced separately to each manipulated variable, starting from an initial steady-state corresponding to a mean NP diameter of 62.98 nm. Fig. 7 depicts the dynamic response of the Ag NPs mean diameter at the exit of the last PFR after the step changes are applied to each manipulated variable. The dynamic responses were discretized with a sampling interval of 1 min to extract the step response coefficients. The number of step response coefficients for each manipulated variable, l_{pin}, must be sufficiently large to capture the entire time window during which the system transitions until it reaches a new steady state. For this system, a time horizon of 20 min is sufficient to capture the entire dynamic response of the mean NP diameter, resulting in step response models containing 21 coefficients for each manipulated variable (see Eq. (19)). The prediction of the mean NP diameter at time instance $t + k$ is a summation of the impact of all manipulated input flows individually. In this case, Eq. (20) is presented in more details as follows (Eq. (30)), where $\hat{y_1}$ corresponds to the Ag NP mean diameter and $n_u = 6$:

$$\hat{y_1}(t+k|t) = \sum_{j=1}^{n_u}\sum_{i=1}^{k} g_{i,j}\Delta u_j(t+k-i) + \\ + \sum_{j=1}^{n_u}\sum_{i=1}^{l_{pin}}((g_{k+i,j} - g_{i,j})\Delta u_j(t-i)) + y_{1,m}(t) - y_{1,ss}. \quad (30)$$

where $g_{i,j}$ are the step response coefficients corresponding to input j.

To facilitate computations at all discrete time points during the prediction horizon N_p, Eq. (30) is evolved into Eq. (31), which provides the predictions of the output variable across N_p as a vector:

$$\begin{bmatrix} \hat{y}_1(t+1|t) \\ \vdots \\ \hat{y}_1(t+N_p|t) \end{bmatrix} = \sum_{j=1}^{n_u}\left[G_j \begin{bmatrix} \Delta u_j(t) \\ \vdots \\ \Delta u_j(t+N_c) \end{bmatrix} + Fr_j \begin{bmatrix} \Delta u_j(t-1) \\ \vdots \\ \Delta u_j(t-l_{pin}) \end{bmatrix}\right] + \begin{bmatrix} y_{1,m}(t) - y_{1,ss} \\ \vdots \\ y_{1,m}(t) - y_{1,ss} \end{bmatrix}. \quad (31)$$

Eq. (31) contains two matrices of appropriate dimensions for each manipulated variable: The matrix G_j is multiplied by the vector containing the future incremental changes of the manipulated variable over the control horizon $[\Delta u_j(t) \ldots \Delta u_j(t+N_c)]$. Thus, G_j has dimensions $N_p \times (N_c + 1)$. The matrix Fr_j is multiplied by the vector containing the past changes of the manipulated variable $[\Delta u_j(t-1) \ldots \Delta u_j(t-l_{pin})]$. Therefore, Fr_j has dimensions $N_p \times l_{pin}$.

Step response models are reduced order models incorporated into the DMC algorithm, which inevitably introduce some discrepancies compared to the more detailed MOM physics-based model. To assess how this modeling uncertainty affects the accuracy of step response model predictions, a +20% step change was applied to all manipulated variables from the initial steady-state condition to both the MOM model and the step response models. Fig. 8 shows the results. As anticipated, prediction errors occur as the system moves further from the initial steady-state condition. Nevertheless, the step response models continue to adequately reflect the system's dynamic behavior, even in areas distant from the original linearization point.

Once the step response models were developed, the next step involved defining the DMC optimization problem. To capture the main ideas from the earlier sections, the complete mathematical formulation of this problem for a control system with two controlled variables is

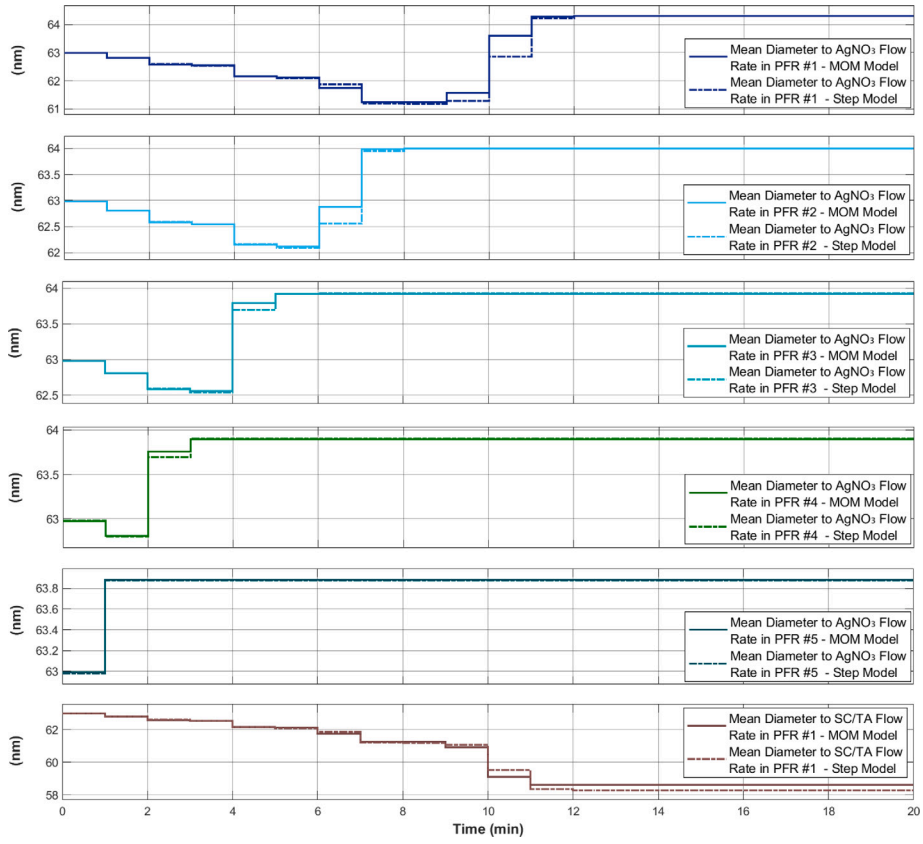

Fig. 8. Dynamic responses of NP mean diameter and predictions of the step response models corresponding to 20% step changes in the manipulated variables.

presented in the following equations:

$$\min_{(\Delta u(t),\ldots,\Delta u(t+N_c))} \left\{ \sum_{k=1}^{N_p} \left\| \begin{bmatrix} \hat{y}_1(t+k|t) - y_{sp,1} \\ \hat{y}_2(t+k|t) - y_{sp,2} \end{bmatrix} \right\|_Q^2 + \sum_{k=0}^{N_c} \left\| \Delta u(t+k) \right\|_R^2 + \right.$$
$$+ W_{min,1} \sum_{k=1}^{N_p} \epsilon_{min,1}(t+k) + W_{max,1} \sum_{k=1}^{N_p} \epsilon_{max,1}(t+k) + \quad (32)$$
$$\left. W_{min,2} \sum_{k=1}^{N_p} \epsilon_{min,2}(t+k) + W_{max,2} \sum_{k=1}^{N_p} \epsilon_{max,2}(t+k) \right\}$$

subject to:

$$\begin{bmatrix} \hat{y}_1(t+1|t) \\ \vdots \\ \hat{y}_1(t+N_p|t) \end{bmatrix} = \sum_{j=1}^{6} \left[G_j \begin{bmatrix} \Delta u_j(t) \\ \vdots \\ \Delta u_j(t+N_c) \end{bmatrix} + Fr_j \begin{bmatrix} \Delta u_j(t-1) \\ \vdots \\ \Delta u_j(t-l_{pin}) \end{bmatrix} \right] + \begin{bmatrix} y_{1,m}(t) - y_{1,ss} \\ \vdots \\ y_{1,m}(t) - y_{1,ss} \end{bmatrix} \quad (33)$$

$$\hat{y}_2(t+k|t) = -3 \cdot 10^{-5} \cdot \hat{y}_1(t+k|t)^2 - 8 \cdot 10^{-4} \cdot \hat{y}_1(t+k|t) + 0.4845,\ k = 1,\ldots,N_p \quad (34)$$

$$\Delta u(t+k) = [\Delta u_1(t+k), \Delta u_2(t+k), \ldots, \Delta u_6(t+k)],\ k = 0,\ldots,N_c \quad (35)$$

$$\Delta u_j(t+k) = u_j(t+k) - u_j(t+k-1),\ j = 1,\ldots,6,\ k = 0,\ldots,N_c \quad (36)$$

$$u_{min,j} \le u_j(t+k) \le u_{max,j},\ j = 1,\ldots,6,\ k = 0,\ldots,N_c \quad (37)$$

$$y_{min,j} - \epsilon_{min,j}(t+k) \le \hat{y}_j(t+k|t) \le y_{max,j} + \epsilon_{max,j}(t+k),\ j = 1,2,\ k = 1,\ldots,N_p \quad (38)$$

$$\epsilon_{min,j}(t+k), \epsilon_{max,j}(t+k) \ge 0,\ j = 1,2,\ k = 1,\ldots,N_p. \quad (39)$$

The control algorithm aims to minimize the objective function given in Eq. (32) while adhering to the constraints specified in Eqs. (33)–(39). For the implementation of the algorithm, CasADi, an open-source software tool for numerical optimization (Andersson et al., 2019), was utilized (version 3.6.3). CasADi employs a symbolic framework to model and solve optimization problems, which supports the formulation of optimal control problems. Among the various solvers available within CasADi, IPOPT was selected (Andersson et al., 2019), a widely used open-source primal–dual interior point method, which is included in CasADi installations.

4.4.1. Closed-loop simulation platform

The closed-loop simulation platform builds upon the open-loop simulator by incorporating DMC to establish a control feedback loop. Fig. 9 illustrates the closed-loop simulator within the MATLAB-Simulink environment. The controller receives the current measurements of the mean diameter and ToxScore of the Ag NPs in the product stream, along with their set-points, bounds, and a set of parameters that adjust the optimization problem. This information is used to construct the parameter vector for the optimization problem formulation in CasADi. The parameters are updated at each discrete time step to provide DMC with up-to-date information on the system's state and control objectives. The controller outputs a vector with six elements, containing the optimal incremental changes for the six manipulated flows relative to the current values. The closed-loop simulator is an interactive simulation platform that consists of the closed-loop system and the control panel (Fig. 10). The final stages of control design involve fine-tuning the parameters of the DMC controller to improve its performance, a process carried out through trial and error. The results of this parameter tuning process are presented in Table 2. It should be noted that the formulation of the DMC problem permits the specification of a set-point for ToxScore. However, in most instances, this feature is not activated and only the upper bound on the Toxscore is applied. In such cases, q_{22} is set equal to 0.

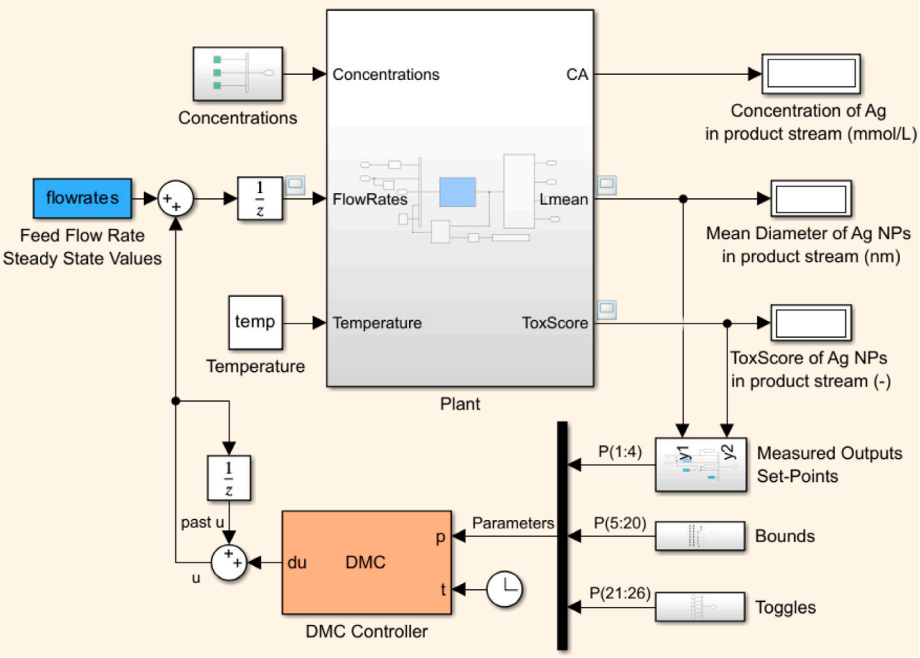

Fig. 9. Closed-Loop dynamic simulator.

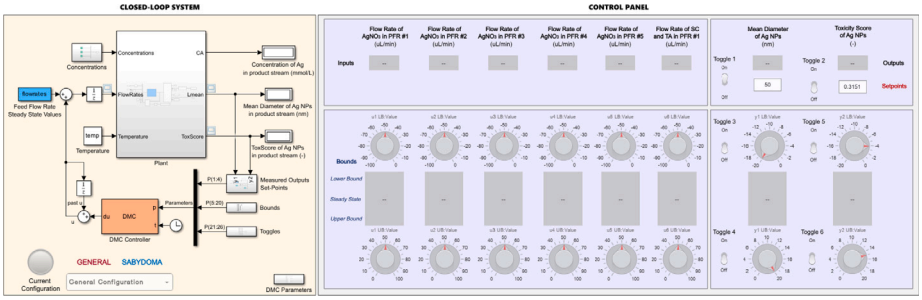

Fig. 10. Closed-Loop simulation platform.

Table 2
Parameter Tuning for DMC Controller in general configuration.

Controller parameters	
Prediction Horizon	$N_p = 20$
Control Horizon	$N_c = 10$
Sample Time	$T_s = 1$ min
Weighting matrix	Q: $q_{ij,i\neq j} = 0$, $q_{11} = 10$, $q_{22} = 10^5$
Weighting matrix	R: $r_{ij,i\neq j} = 0$, $r_{ij,i=j} = 0.1$
Penalty weights for CV1	$W_{min,1} = 10^4$, $W_{max,1} = 10^4$
Penalty weights for CV2	$W_{min,2} = 10^6$, $W_{max,2} = 10^6$

4.4.2. Closed-loop simulation results

The effectiveness of the control algorithm is typically assessed through its performance in two main control tasks: disturbance rejection and set-point tracking. To showcase the efficiency of the proposed control framework, simulations of two representative case studies were performed. The dynamic responses of the process variables are displayed using the visualization tools provided by the simulation platform.

The first case study illustrates the control system's response to a simultaneous +20% step change in the concentrations of SC and TA in the inlet stream to the first PFR. The results of the simulation are depicted in Fig. 11. The top two subplots display the controlled variables, the third subplot illustrates the adjustments in the manipulated variables, and the bottom subplot shows the step changes in the unmeasured disturbances along with their timing.

The results clearly demonstrate that the controller effectively rejects the unmeasured disturbances and returns the system to its initial steady state. Since higher concentrations of reducing agents result in smaller NPs, the controller reduces the flow rate of the corresponding stream (SC/TA flow in PFR #1, 3rd subplot of Fig. 11). It also prioritizes increasing the flow rate of $AgNO_3$ into the final PFRs to achieve faster results. This control strategy balances the trade-off between overshoot and convergence by leveraging the residence time information provided by the step response models.

In addition to disturbance rejection, the control algorithm also facilitates set-point tracking. Fig. 12 shows the control actions implemented by DMC when a set-point of 50 nm is specified for the NP mean diameter, starting from the same initial conditions like the previous case study. Note that in this simulation, the upper bound on the ToxScore has been deactivated in the DMC problem setup.

The results demonstrate the controller's ability to guide the system to the desired set-point value with zero offset, while continuously respecting the upper and lower bounds of the manipulated variables. This is clearly illustrated in the third subplot of Fig. 12, where the flow rate values consistently remain within the operational limits, which are indicated by the black dashed lines. However, the ToxScore values

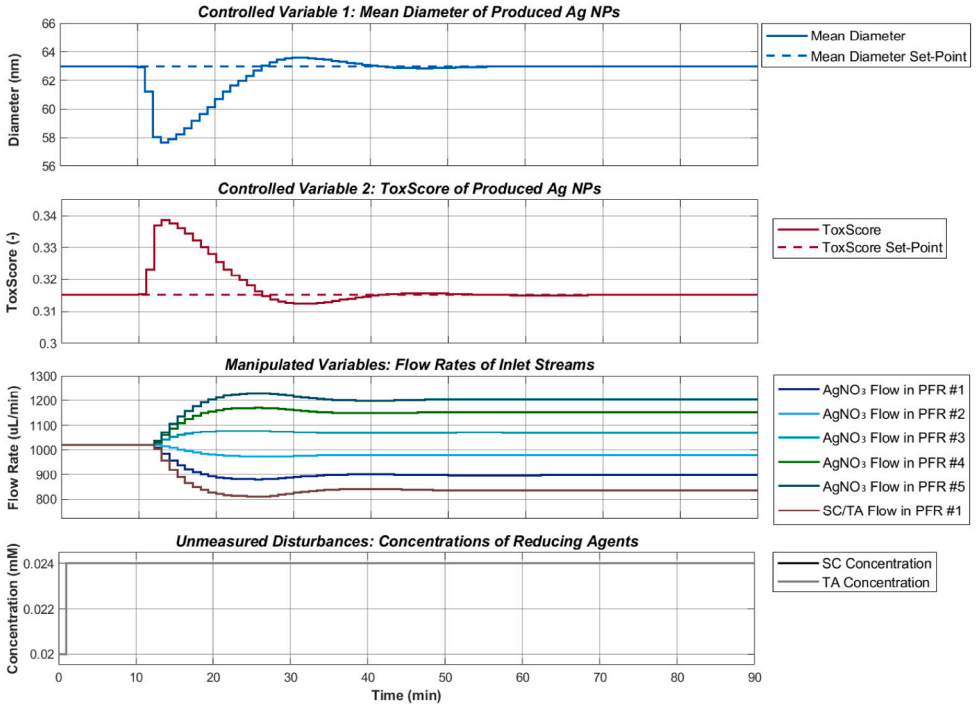

Fig. 11. Dynamic response of the closed-loop system in rejecting unmeasured disturbances in SC and TA concentration.

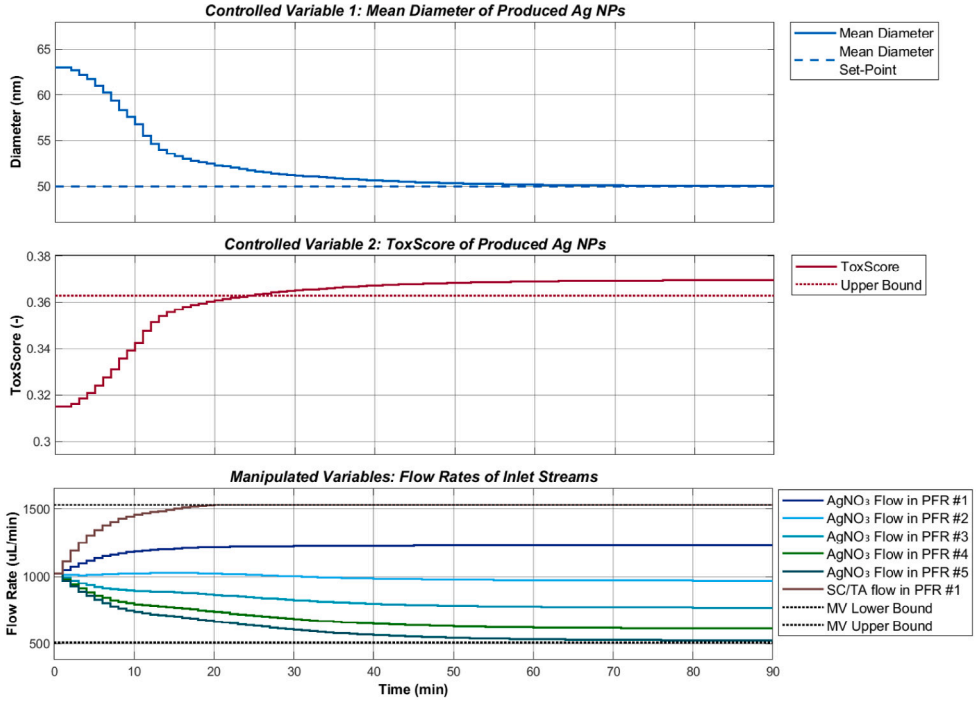

Fig. 12. Dynamic response of the closed-loop system in tracking a set-point of 50 nm for the mean NP diameter without activating the upper ToxScore bound.

exceed the safety threshold, as shown in the second subplot, because the corresponding upper bound was deactivated.

Fig. 13 illustrates how the results change when the upper bound on the ToxScore is activated to prevent conditions that could lead to the production of NPs with undesirable safety characteristics. The dynamic responses now show that the Toxscore values do not violate the safety threshold; however, as a result, the diameter does not exactly match the desired set-point.

4.4.3. Closed-loop simulation results considering modeling and measurement uncertainties

Model uncertainty is already accounted in the DMC control scheme, addressing the discrepancy between the step response model predicting the NP mean diameter in the DMC controller formulation and the detailed MOM model. To further demonstrate the robustness of the proposed framework, a modified ToxScore predictive model was used within DMC, while assuming that the original model Eq. (29) represents the actual ToxScore metric. Specifically, the coefficients in Eq. (29)

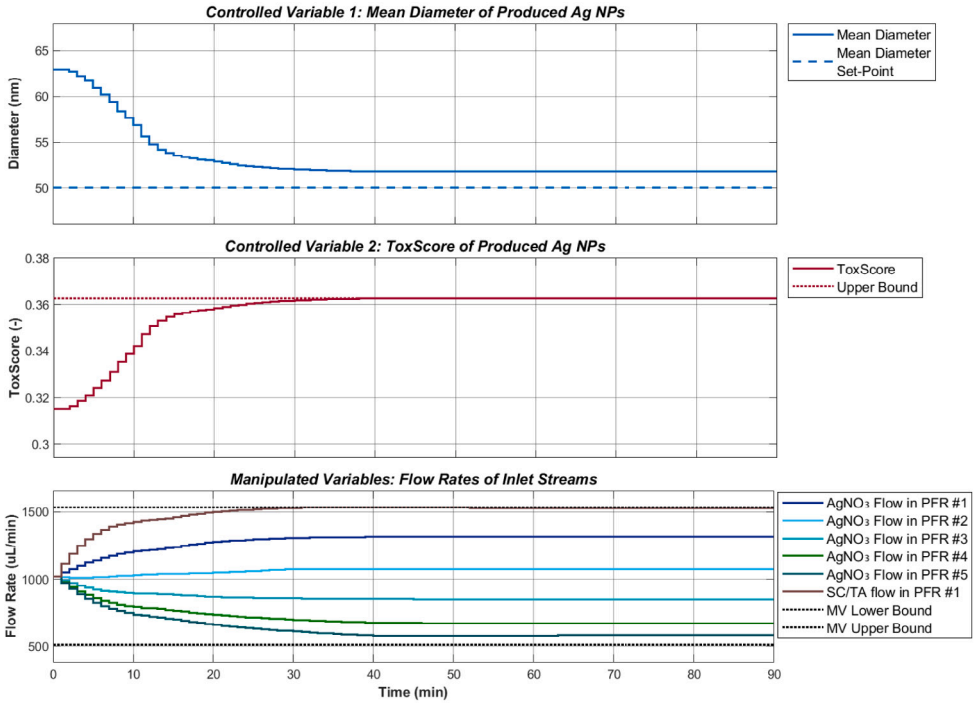

Fig. 13. Dynamic response of the closed-loop system in tracking a set-point of 50 nm for the mean NP diameter with an activated upper bound for ToxScore.

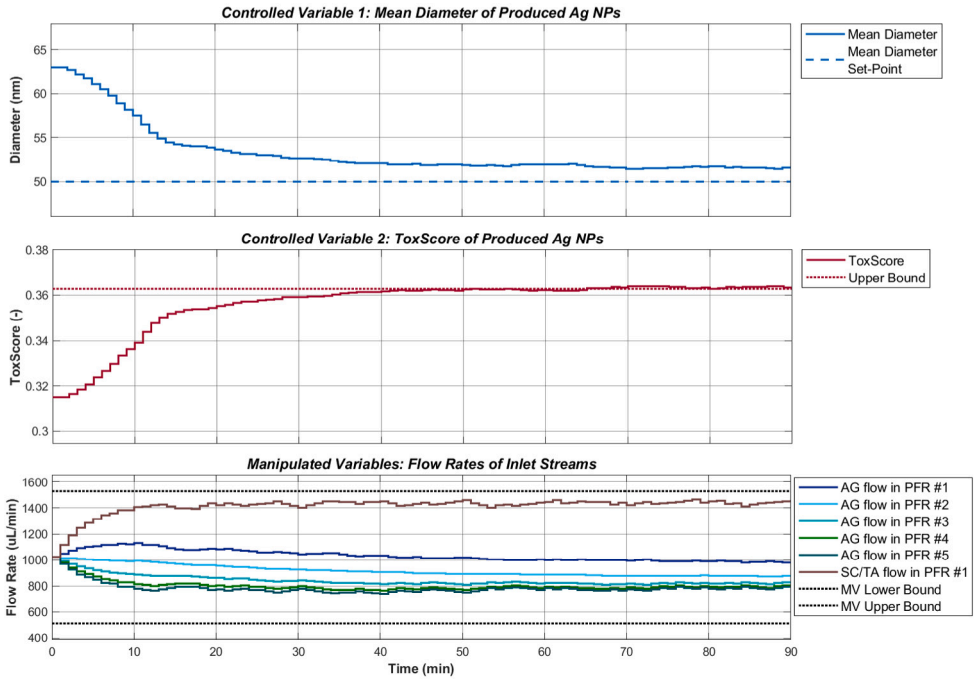

Fig. 14. Dynamic response of the closed-loop system in tracking a set-point of 50 nm for the mean NP diameter with an activated upper bound for ToxScore, accounting for uncertainty in the ToxScore prediction model.

were modified to create the ToxScore prediction model used in DMC, as shown in Eq. (40):

$$ToxScore = -4.31 \cdot 10^{-5} \cdot D^2 - 9.58 \cdot 10^{-4} \cdot D + 0.3880. \quad (40)$$

After this modification, the set-point tracking problem previously presented in Fig. 13 was simulated again. The only tuning parameter that was changed was the weight that penalizes violations of the ToxScore upper bound, which was set to $W_{max,2} = 10^{10}$. It is demonstrated that the DMC controller successfully stabilizes the system in a new steady state that adheres to the ToxScore restrictions (Fig. 14). Compared to Fig. 13, slight fluctuations are observed in both the manipulated and the controlled variables.

Measurement uncertainties were considered, by introducing Gaussian noise into the plant output signals that are provided as feedback to the controller. Gaussian noise is characterized by a probability density function with a mean value $\mu = 0$ and a standard deviation σ, which determines the magnitude of the uncertainty. Gaussian noise with $\mu = 0, \sigma = 1$ was added to diameter measurements, while Gaussian noise

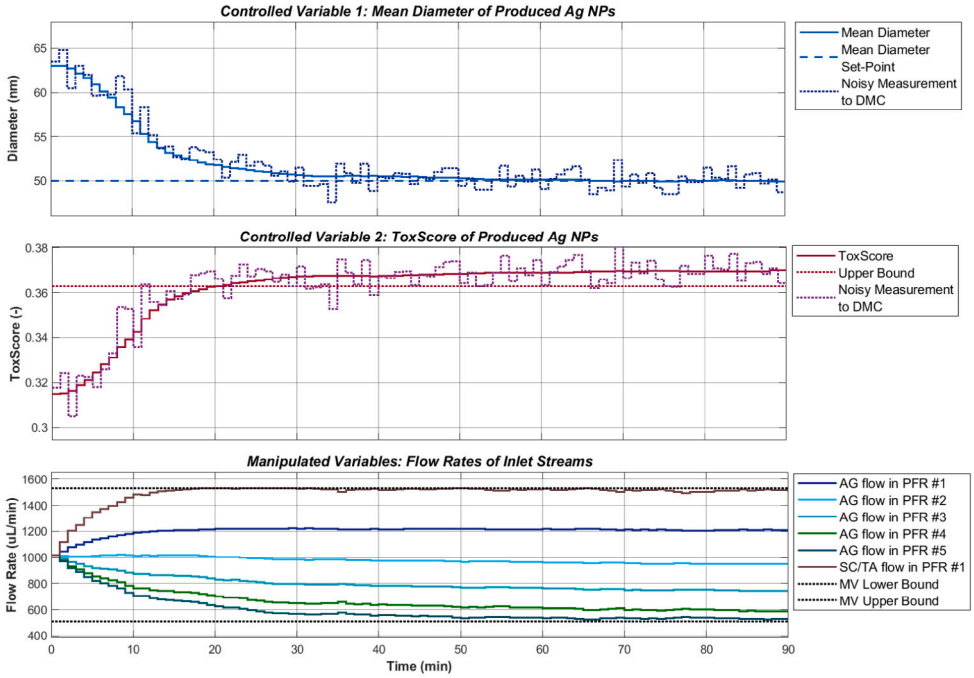

Fig. 15. Dynamic response of the closed-loop system in tracking a set-point of 50 nm for the mean NP diameter without activating the upper ToxScore bound, accounting for ToxScore model uncertainty and measurement uncertainties.

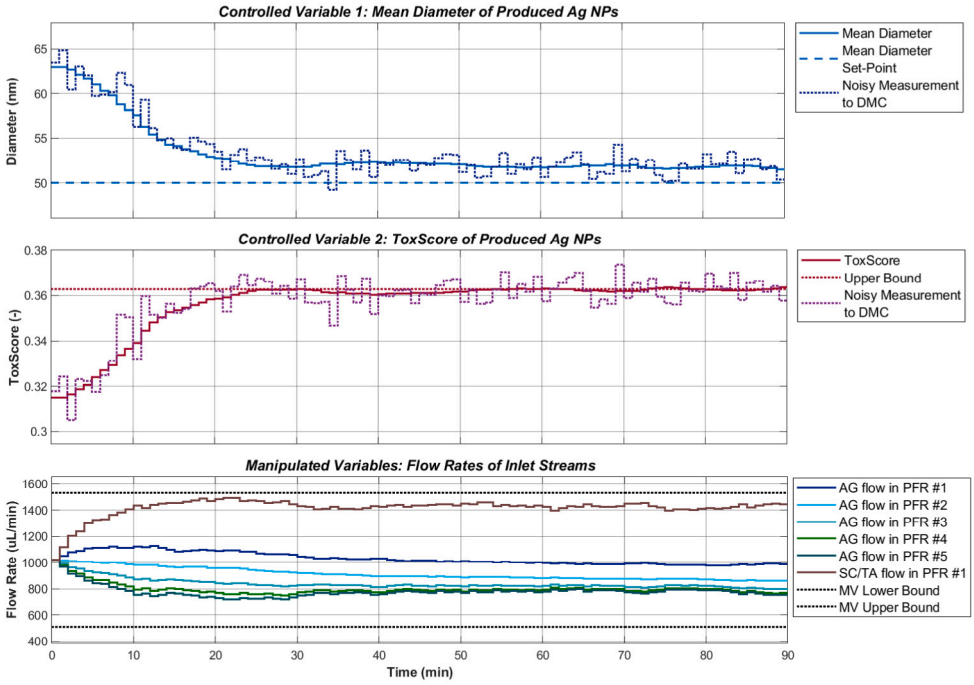

Fig. 16. Dynamic response of the closed-loop system in tracking a set-point of 50 nm for the mean NP diameter with an activating upper bound for ToxScore, accounting for ToxScore model uncertainty and measurement uncertainties.

with $\mu = 0, \sigma = 5 \cdot 10^{-3}$ was added to ToxScore measurements to account for intrinsic variability and sensor inaccuracies.

The case studies corresponding to Figs. 12 and 13 were re-examined, now considering both ToxScore model uncertainty and measurement uncertainties. The results are presented in Figs. 15 and 16. It is illustrated that the presence of modeling and measurement uncertainties does not affect significantly the performance of the control framework, which still manages to track the mean diameter of the produced NPs to the desired set-point in the first case and keep the ToxScore metric within the safety bounds in the second simulation.

The code that generated the reported results can be found in: https://github.com/ntua-unit-of-control-and-informatics/mpc-sabydoma. The experimental data used for developing the ToxScore inferential sensor and for estimating the kinetic parameters in the population balance model can be available upon request.

5. Conclusions

This study introduces the SbPC framework, a novel process control approach for regulating the morphological and safety characteristics of NMs during continuous production. The framework integrates dynamic first-principles modeling, real-time toxicity monitoring, and advanced MPC-based process control. A population balance model employing the MOM approximation provides a detailed understanding of nucleation and growth dynamics, enabling predictions of NP size and size distribution throughout the reactors and at the production process's exit. This model serves as the basis for deriving step-response models used in developing the MPC controller. The integration of a data-driven toxicity prediction model facilitates real-time health hazard assessment based on NP size. The MPC controller is designed to meet the functionality requirements defined by the desired size of the produced NPs while ensuring that the safety characteristics of the produced NPs remain within acceptable limits. Through a case study involving a continuous Ag NP production system, the framework demonstrated its ability to regulate critical morphological and safety characteristics in real-time. In this case study, the kinetic parameters of the population balance model were estimated by fitting the model to experimental data using the TSEMO multi-objective optimization method. Through an extensive set of simulations, it was demonstrated that functionality and safety requirements, which can present conflicting objectives, can be effectively balanced over short timeframes. It was also shown that the proposed framework remains efficient even in the presence of model uncertainties and measurement errors. The proposed SbPC framework addresses existing gaps in the nanotechnology field and lays a foundation for implementing SSbD principles in NM manufacturing. Its modular design makes the SbPC framework a scalable solution applicable to the production of various NMs, including gold, aluminum (Manikam et al., 2011), copper (Lee et al., 2008; Khan et al., 2016), and zinc (Hachem et al., 2022) NPs, thereby broadening its industrial relevance.

CRediT authorship contribution statement

Argyri Kardamaki: Writing – original draft, Visualization, Validation, Software, Methodology, Investigation, Formal analysis, Data curation, Conceptualization. **Athanassios Nikolakopoulos:** Writing – original draft, Visualization, Validation, Software, Methodology, Investigation, Formal analysis, Data curation, Conceptualization. **Mihalis Kavousanakis:** Writing – review & editing, Writing – original draft, Validation, Supervision, Software, Methodology, Investigation, Formal analysis, Conceptualization. **Philip Doganis:** Writing – original draft, Visualization, Validation, Software, Methodology, Investigation, Formal analysis, Data curation, Conceptualization. **Matt Jellicoe:** Writing – original draft, Validation, Methodology, Investigation, Data curation. **William Stokes:** Writing – original draft, Validation, Methodology, Investigation, Data curation. **Vesa Hongisto:** Writing – original draft, Visualization, Validation, Methodology, Investigation, Data curation. **Matthew Simmons:** Writing – original draft, Validation, Methodology, Investigation, Data curation. **Thomas W. Chamberlain:** Writing – review & editing, Supervision, Methodology, Investigation, Formal analysis. **Nikil Kapur:** Writing – review & editing, Supervision, Methodology, Investigation. **Roland Grafström:** Writing – review & editing, Supervision, Methodology, Investigation. **Andrew Nelson:** Writing – review & editing, Validation, Supervision, Methodology, Investigation, Funding acquisition, Conceptualization. **Haralambos Sarimveis:** Writing – review & editing, Writing – original draft, Supervision, Software, Methodology, Investigation, Funding acquisition, Formal analysis, Conceptualization.

Declaration of competing interest

The authors declare the following financial interests/personal relationships which may be considered as potential competing interests: Haralambos Sarimveis reports financial support was provided by European Commission. Argyri Kardamaki reports financial support was provided by European Commission. Athanassios Nikolakopoulos reports financial support was provided by European Commission. Mihalis Kavousanakis reports financial support was provided by European Commission. Philip Doganis reports financial support was provided by European Commission. Matt Jellicoe reports financial support was provided by European Commission. William Stokes reports financial support was provided by European Commission. Vesa Hongisto reports financial support was provided by European Commission. Thomas W. Chamberlain reports financial support was provided by European Commission. Matthew Simmons reports financial support was provided by European Commission. Nikil Kapur reports financial support was provided by European Commission. Roland Grafstrom reports financial support was provided by European Commission. Andrew Nelson reports financial support was provided by European Commission. If there are other authors, they declare that they have no known competing financial interests or personal relationships that could have appeared to influence the work reported in this paper.

Acknowledgment

This work has been funded by the European Commission under the HORIZON 2020 project SABYDOMA (Grant Agreement no. 862296).

Data availability

A link to a GitHub repository is provided where the code is available.

References

Abou El-Nour, K.M., Eftaiha, A., Al-Warthan, A., Ammar, R.A., 2010. Synthesis and applications of silver nanoparticles. Arab. J. Chem. 3 (3), 135–140.

Acharya, D., Singha, K.M., Pandey, P., Mohanta, B., Rajkumari, J., Singha, L.P., 2018. Shape dependent physical mutilation and lethal effects of silver nanoparticles on bacteria. Sci. Rep. 8 (1), 201.

Akter, M., Sikder, M.T., Rahman, M.M., Ullah, A.A., Hossain, K.F.B., Banik, S., Hosokawa, T., Saito, T., Kurasaki, M., 2018. A systematic review on silver nanoparticles-induced cytotoxicity: Physicochemical properties and perspectives. J. Adv. Res. 9, 1–16.

Andersson, J.A.E., Gillis, J., Horn, G., Rawlings, J.B., Diehl, M., 2019. CasADi – A software framework for nonlinear optimization and optimal control. Math. Program. Comput. 11 (1), 1–36.

Auclair, J., Gagné, F., 2022. Shape-dependent toxicity of silver nanoparticles on freshwater cnidarians. Nanomaterials 12 (18), 3107.

Bal, V., Bandyopadhyaya, R., 2018. Generalized model for nano-and submicron particle formation in liquid phase, incorporating reaction kinetics and hydrodynamic interaction: Experiment, modeling, and simulation. J. Phys. Chem. C 122 (35), 20489–20499.

Baset, S., Akbari, H., Zeynali, H., Shafie, M., 2011. Size measurement of metal and semiconductor nanoparticles via UV-vis absorption spectra. Dig. J Nanomater. Biostructures 6.

Bentea, L., Watzky, M.A., Finke, R.G., 2017. Sigmoidal nucleation and growth curves across nature fit by the Finke–Watzky model of slow continuous nucleation and autocatalytic growth: explicit formulas for the lag and growth times plus other key insights. J. Phys. Chem. C 121 (9), 5302–5312.

Beyene, H.D., Werkneh, A.A., Bezabh, H.K., Ambaye, T.G., 2017. Synthesis paradigm and applications of silver nanoparticles (AgNPs), a review. Sustain. Mater. Technol. 13, 18–23.

Bosetti, L., Mazzotti, M., 2019. Population balance modeling of growth and secondary nucleation by attrition and ripening. Cryst. Growth & Des. 20 (1), 307–319.

Bradford, E., Schweidtmann, A.M., Lapkin, A., 2018. Efficient multiobjective optimization employing Gaussian processes, spectral sampling and a genetic algorithm. J. Global Optim. 71 (2), 407–438.

Caldeira, C., Farcal, L.R., Garmendia Aguirre, I., Mancini, L., Tosches, D., Amelio, A., Rasmussen, K., Rauscher, H., Riego Sintes, J., Sala, S., 2022. Safe and sustainable by design chemicals and materials – Framework for the definition of criteria and evaluation procedure for chemicals and materials. Publications Office of the European Union,European Commission and Joint Research Centre.

Camacho, E.F., Bordons, C., Camacho, E.F., Bordons, C., 2007. Introduction to model predictive control. Model. Predict. Control. 1–11.

Casado, C., Pinho, B., Marugán, J., Torrente-Murciano, L., 2023. Predicting the size of silver nanoparticles synthesised in flow reactors: Coupling population balance models with fluid dynamic simulations. Chem. Eng. J. 147684.
Cheng, Y., Wang, F., Fang, C., Su, J., Yang, L., 2016. Preparation and characterization of size and morphology controllable silver nanoparticles by citrate and tannic acid combined reduction at a low temperature. J. Alloys Compd. 658, 684–688.
Cho, Y.-M., Mizuta, Y., Akagi, J.-i., Toyoda, T., Sone, M., Ogawa, K., 2018. Size-dependent acute toxicity of silver nanoparticles in mice. J. Toxicol. Pathol. 31 (1), 73–80.
Cristaldi, D.A., 2020. Continuous-flow Reactors for Large-Scale Production of Nanoparticles (Ph.D. thesis). University of Southampton.
Długosz, O., Banach, M., 2019. Continuous production of silver nanoparticles and process control. J. Cluster Sci. 30 (3), 541–552.
Eremin, Y., 2005. Scattering | scattering theory. In: Guenther, R.D. (Ed.), Encyclopedia of Modern Optics. Elsevier, Oxford, pp. 326–330.
Filbet, F., Laurençot, P., 2004. Numerical simulation of the Smoluchowski coagulation equation. SIAM J. Sci. Comput. 25 (6), 2004–2028.
Gacem, M.A., Abd-Elsalam, K.A., 2022. Strategies for scaling up of green-synthesized nanomaterials: Challenges and future trends. In: Green Synthesis of Silver Nanomaterials. Elsevier, pp. 669–698.
Gao, Y., Pinho, B., Torrente-Murciano, L., 2020. Recent progress on the manufacturing of nanoparticles in multi-phase and single-phase flow reactors. Curr. Opin. Chem. Eng. 29, 26–33.
Gupta, M.C., Ungaro, C., Foley IV, J.J., Gray, S.K., 2018. Optical nanostructures design, fabrication, and applications for solar/thermal energy conversion. Sol. Energy 165, 100–114.
Hachem, K., Ansari, M.J., Saleh, R.O., Kzar, H.H., Al-Gazally, M.E., Altimari, U.S., Hussein, S.A., Mohammed, H.T., Hammid, A.T., Kianfar, E., 2022. Methods of chemical synthesis in the synthesis of nanomaterial and nanoparticles by the chemical deposition method: A review. BioNanoScience 12 (3), 1032–1057.
Hongisto, V., Nymark, P., Kohonen, P.J., Hattara, J., Grafström, R., 2019. High-throughput hazard-based scoring, ranking and grouping of engineered nanomaterials. Toxicol. Lett. 314, S202–S203.
Hulburt, H.M., Katz, S., 1964. Some problems in particle technology: A statistical mechanical formulation. Chem. Eng. Sci. 19 (8), 555–574.
Iravani, S., Korbekandi, H., Mirmohammadi, S.V., Zolfaghari, B., 2014. Synthesis of silver nanoparticles: chemical, physical and biological methods. Res. Pharm. Sci. 9 (6), 385.
Jara, N., Milán, N.S., Rahman, A., Mouheb, L., Boffito, D.C., Jeffryes, C., Dahoumane, S.A., 2021. Photochemical synthesis of gold and silver nanoparticles—A review. Molecules 26 (15), 4585.
Khan, A., Rashid, A., Younas, R., Chong, R., 2016. A chemical reduction approach to the synthesis of copper nanoparticles. Int. Nano Lett. 6, 21–26.
Kong, I.C., Ko, K.-S., Koh, D.-C., 2020. Evaluation of the effects of particle sizes of silver nanoparticles on various biological systems. Int. J. Mol. Sci. 21 (22), 8465.
Kumar, J., Peglow, M., Warnecke, G., Heinrich, S., 2008. An efficient numerical technique for solving population balance equation involving aggregation, breakage, growth and nucleation. Powder Technol. 182 (1), 81–104.
Kumar, J., Warnecke, G., Peglow, M., Heinrich, S., 2009. Comparison of numerical methods for solving population balance equations incorporating aggregation and breakage. Powder Technol. 189 (2), 218–229.
Kwon, J.S.-I., Nayhouse, M., Christofides, P.D., Orkoulas, G., 2014. Modeling and control of crystal shape in continuous protein crystallization. Chem. Eng. Sci. 107, 47–57.
Lee, Y., Choi, J.-r., Lee, K.J., Stott, N.E., Kim, D., 2008. Large-scale synthesis of copper nanoparticles by chemically controlled reduction for applications of inkjet-printed electronics. Nanotechnology 19 (41), 415604.
Lin, Y., Lee, K., Matsoukas, T., 2002. Solution of the population balance equation using constant-number Monte Carlo. Chem. Eng. Sci. 57 (12), 2241–2252.
Liu, H., Li, J., Sun, D., Odoom-Wubah, T., Huang, J., Li, Q., 2014. Modeling of silver nanoparticle formation in a microreactor: reaction kinetics coupled with population balance model and fluid dynamics. Ind. Eng. Chem. Res. 53 (11), 4263–4270.
Makgwane, P.R., Ray, S.S., 2014. Synthesis of nanomaterials by continuous-flow microfluidics: a review. J. Nanosci. Nanotechnol. 14 (2), 1338–1363.
Manikam, V.R., Cheong, K.Y., Razak, K.A., 2011. Chemical reduction methods for synthesizing Ag and Al nanoparticles and their respective nanoalloys. Mater. Sci. Eng.: B 176 (3), 187–203.
Marchisio, D.L., Fox, R.O., 2005. Solution of population balance equations using the direct quadrature method of moments. J. Aerosol Sci. 36 (1), 43–73.
Marvel, S.W., To, K., Grimm, F.A., Wright, F.A., Rusyn, I., Reif, D.M., 2018. ToxPi graphical user interface 2.0: Dynamic exploration, visualization, and sharing of integrated data models. BMC Bioinformatics 19 (1), 80.
McGraw, R., Wright, D.L., 2003. Chemically resolved aerosol dynamics for internal mixtures by the quadrature method of moments. J. Aerosol Sci. 34 (2), 189–209.
Mech, A., Gottardo, S., Amenta, V., Amodio, A., Belz, S., Bøwadt, S., Drbohlavová, J., Farcal, L., Jantunen, P., yska, A.M., Rasmussen, K., Riego Sintes, J., Rauscher, H., 2022. Safe- and sustainable-by-design: The case of smart nanomaterials. A perspective based on a European workshop. RTP 128, 105093.
Mie, G., 1908. A contribution to the optics of turbid media, especially colloidal metallic suspensions. Ann. Phys. 25, 377–445.
Mulholland, M., 2016. Applied Process Control: Essential Methods. John Wiley & Sons.
Nelson, A., 2022. An innovative approach to dealing with the safety-by-design issue–SABYDOMA. Toxicol. Lett. 368, S14–S79.
Niskanen, I., Forsberg, V., Zakrisson, D., Reza, S., Hummelgård, M., Andres, B., Fedorov, I., Suopajärvi, T., Liimatainen, H., Thungström, G., 2019. Determination of nanoparticle size using Rayleigh approximation and Mie theory. Chem. Eng. Sci. 201, 222–229.
Noga, M., Milan, J., Frydrych, A., Jurowski, K., 2023. Toxicological aspects, safety assessment, and green toxicology of silver nanoparticles (AgNPs)—critical review: state of the art. Int. J. Mol. Sci. 24 (6), 5133.
OECD, 2022. Sustainability and safe and sustainable by design: Working descriptions, series on the safety of manufactured nanomaterials no. 105 for the safer innovation approach.
Owen, J., Kuznecovs, M., Bhamji, R., William, N., Domenech-Garcia, N., Hesler, M., Knoll, T., Kohl, Y., Nelson, A., Kapur, N., 2020. High-throughput electrochemical sensing platform for screening nanomaterial–biomembrane interactions. Rev. Sci. Instrum. 91 (2).
Panzarini, E., Mariano, S., Carata, E., Mura, F., Rossi, M., Dini, L., 2018. Intracellular transport of silver and gold nanoparticles and biological responses: an update. Int. J. Mol. Sci. 19 (5), 1305.
Pico, P., Nathanael, K., Lavino, A.D., Kovalchuk, N.M., Simmons, M.J., Matar, O.K., 2023. Silver nanoparticles synthesis in microfluidic and well-mixed reactors: A combined experimental and PBM-CFD study. Chem. Eng. J. 474, 145692.
Pinho, B., Torrente-Murciano, L., 2020. Continuous manufacturing of silver nanoparticles between 5 and 80 nm with rapid online optical size and shape evaluation. React. Chem. Eng. 5 (2), 342–355.
Pinho, B., Torrente-Murciano, L., 2021. Dial-a-particle: Precise manufacturing of plasmonic nanoparticles based on early growth information—Redefining automation for slow material synthesis. Adv. Energy Mater. 11 (32), 2100918.
Prabhu, S., Poulose, E.K., 2012. Silver nanoparticles: mechanism of antimicrobial action, synthesis, medical applications, and toxicity effects. Int. Nano Lett. 2 (1), 32.
Prakash, B., Katoch, V., Shah, A., Sharma, M., Devi, M.M., Panda, J.J., Sharma, J., Ganguli, A.K., 2020. Continuous flow reactor for the controlled synthesis and inline photocatalysis of antibacterial Ag_2S nanoparticles. Photochem. Photobiol. 96 (6), 1273–1282.
Ramkrishna, D., 2000. Population Balances: Theory and Applications to Particulate Systems in Engineering. Elsevier.
Ramkrishna, D., Singh, M.R., 2014. Population balance modeling: current status and future prospects. Annu. Rev. Chem. Biomol. Eng. 5, 123–146.
Randolph, A., 2012. Theory of Particulate Processes: Analysis and Techniques of Continuous Crystallization. Elsevier.
Reif, D.M., Martin, M.T., Tan, S.W., Houck, K.A., Judson, R.S., Richard, A.M., Knudsen, T.B., Dix, D.J., Kavlock, R.J., 2010. Endocrine profiling and prioritization of environmental chemicals using ToxCast data. Environ. Health Perspect. 118 (12), 1714–1720.
Saldanha, P.L., Lesnyak, V., Manna, L., 2017. Large scale syntheses of colloidal nanomaterials. Nano Today 12, 46–63.
Sánchez Jiménez, A., Puelles, R., Perez-Fernandez, M., Barruetabeña, L., Jacobsen, N.R., Suarez-Merino, B., Micheletti, C., Manier, N., Salieri, B., Hischier, R., Tsekovska, R., Handzhiyski, Y., Bouillard, J., Oudart, Y., Galea, K.S., Kelly, S., Shandilya, N., Goede, H., Gomez-Cordon, J., Jensen, K.A., van Tongeren, M., Apostolova, M.D., Llopis, I.R., 2022. Safe(r) by design guidelines for the nanotechnology industry. NanoImpact 25, 100385.
Sandoe, H.E., Watzky, M.A., Diaz, S.A., 2019. Experimental probes of silver metal nanoparticle formation kinetics: Comparing indirect versus more direct methods. Int. J. Chem. Kinet. 51 (11), 861–871.
Sasidharan, S., Raj, S., Sonawane, S., Sonawane, S., Pinjari, D., Pandit, A., Saudagar, P., 2019. Nanomaterial synthesis: chemical and biological route and applications. In: Nanomaterials Synthesis. Elsevier, pp. 27–51.
Sharma, N.K., Vishwakarma, J., Rai, S., Alomar, T.S., AlMasoud, N., Bhattarai, A., 2022. Green route synthesis and characterization techniques of silver nanoparticles and their biological adeptness. ACS Omega 7 (31), 27004–27020.
Syafiuddin, A., Salmiati, Salim, M.R., Beng Hong Kueh, A., Hadibarata, T., Nur, H., 2017. A review of silver nanoparticles: research trends, global consumption, synthesis, properties, and future challenges. J. Chin. Chem. Soc. 64 (7), 732–756.
Tahir, F., Krzemieniewska-Nandwani, K., Mack, J., Lovett, D., Siddique, H., Mabbott, F., Raval, V., Houson, I., Florence, A., 2017. Advanced control of a continuous oscillatory flow crystalliser. Control Eng. Pract. 67, 64–75.
Tak, Y.K., Pal, S., Naoghare, P.K., Rangasamy, S., Song, J.M., 2015. Shape-dependent skin penetration of silver nanoparticles: does it really matter? Sci. Rep. 5 (1), 16908.
Tatjewski, P., 2007. Advanced Control of Industrial Processes: Structures and Algorithms. Springer Science & Business Media.
Thanh, N.T., Maclean, N., Mahiddine, S., 2014. Mechanisms of nucleation and growth of nanoparticles in solution. Chem. Rev. 114 (15), 7610–7630.
Vetter, T., Iggland, M., Ochsenbein, D.R., Hänseler, F.S., Mazzotti, M., 2013. Modeling nucleation, growth, and Ostwald ripening in crystallization processes: a comparison between population balance and kinetic rate equation. Cryst. Growth & Des. 13 (11), 4890–4905.

Waktole, G., 2023. Toxicity and molecular mechanisms of actions of silver nanoparticles. J. Biomater. Nanobiotechnology 14 (3), 53–70.
Yaqoob, A.A., Umar, K., Ibrahim, M.N.M., 2020. Silver nanoparticles: various methods of synthesis, size affecting factors and their potential applications–a review. Appl. Nanosci. 10, 1369–1378.
Zhang, J., Wang, F., Yalamarty, S.S.K., Filipczak, N., Jin, Y., Li, X., 2022. Nano silver-induced toxicity and associated mechanisms. Int. J. Nanomedicine 1851–1864.
Zhu, H., Wu, K.-J., He, C.-H., 2021. Continuous synthesis of uniformly dispersed mesoporous SBA-15 supported silver nanoparticles in a coiled flow inverter reactor. Front. Chem. 9, 747105.